2019 IEEE 58th Conference on Decision and Control (CDC)
Palais des Congrès et des Expositions Nice Acropolis
Nice, France, December 11-13, 2019

Optimal control of stacked multi-kite systems for utility-scale airborne wind energy

Jochem De Schutter[1], Rachel Leuthold[1], Thilo Bronnenmeyer[2], Reinhart Paelinck[2], Moritz Diehl[1]

Abstract— **Within the prevailing single-kite paradigm, the current roadmap towards utility-scale airborne wind energy (AWE) involves building ever larger aircraft. Consequently, utility-scale AWE systems increasingly suffer from similar upscaling drawbacks as conventional wind turbines. In this paper, an alternative upscaling strategy based on stacked multi-kite systems is proposed. Although multi-kite systems are well-known in the literature, the consideration of stacked configurations extends the design space even further and could allow for significantly smaller aircraft, and therefore possibly to cheaper, mass-producible utility-scale AWE systems. To assess the potential of the stacking concept, optimal control is applied to optimize both system design and flight trajectories for a range of configurations, at two different industry-relevant wind sites. The results show that the modular stacking concept effectively decouples aircraft wing sizing considerations from the total power output demand. An efficiency increase of up to 20% is reported when the harvesting area for the same amount of aircraft is doubled using a stacked configuration. Moreover, it is shown that stacked configurations can more than halve the peak power overshoot within one power cycle with respect to conventional single-kite systems.**

I. INTRODUCTION

Airborne wind energy (AWE) is an emerging renewable energy technology that aims to harvest high-altitude wind power at a fraction of the cost and material of conventional wind turbines. It is based on the concept, first investigated in [11], of a tethered aircraft - a "kite" - flying fast crosswind manoeuvres at high altitudes, thereby tapping into strong and steady winds that conventional wind turbines cannot reach.

In order to compete in the utility market, AWE systems in the MW range need to be developed and made economically viable. The upscaling strategy currently dominating in industry is based on single-kite systems and entails increasing aircraft size until the desired power output is reached. The largest existing single-kite system known to date is a 600 kW system with 30 m wing span [12]. Recently, leading companies in the field have presented plans to develop 4 MW and 5 MW systems with 50 m [7] and 65 m wing span respectively [12].

This upscaling strategy intrinsically involves many of the disadvantages associated with large-scale conventional wind turbines: expensive system production, transport, maintenance, repair, intricate structural mechanics, etc. These drawbacks limit the relative electricity price improvement that can be achieved by an AWE system.

There are however alternative strategies. Multi-kite AWE systems (MAWES), first envisaged in [13], are based on the idea of multiple aircraft flying in crosswind, balancing their forces so as to minimize their shared main tether's lateral motion. Initial studies on dual-kite systems based on optimal control using point-mass models predict an efficiency increase of at least factor two [16] for large-scale systems, and a factor 1.7 when induction effects are taken into account [17].

Single-layer multi-kite systems have a bounded potential however. The steady-state study [9] predicts that multi-kite efficiency decreases with the number of kites per layer. Additionally, safety prohibits many aircraft flying close to each other. Hence the idea of stacking multi-kite systems by extending the main tether, as shown in Fig, 1, thereby naturally increasing the total harvesting area as the number of aircraft in the system grows. A stack-based upscaling concept for AWE based on networked rotary ring kites and tensile rotary power transfer is proposed in [14]. However no simulation data are available on the performance of this system in the MW range.

This paper investigates the performance of utility-scale stacked multi-kite systems relative to single-layer single- and multi-kite systems. The system class under consideration is that of rigid-wing pumping type systems. Optimal control is applied to compute optimal system designs and flight trajectories for different multi-kite configurations, tailored to two industry-relevant wind sites with related power demand. The different configurations are then compared in terms of flight trajectory and aircraft sizing.

Section II states optimization-friendly system dynamics and path constraints. Section III describes the parametric optimal control problem (OCP) used for trajectory optimization and Section IV presents the case study results, while Section V poses some conclusions.

II. SYSTEM MODEL

The system model incorporates 6 DOF aircraft dynamics, tether tension and drag forces, induction effects, wind shear modeling and the atmospheric density drop. It has been presented in detail for single-layer MAWES in [8]. In this section, we summarize this model and augment it with additional assumptions for the multi-layer case as well as with some mass scaling laws.

[1]Systems Control and Optimization Laboratory, Department of Microsystems Engineering (IMTEK) and Department of Mathematics, University of Freiburg, Georges-Koehler-Allee 102, 79110 Freiburg, Germany. jochem.de.schutter@imtek.de, rachel.colette.leuthold@imtek.uni-freiburg.de, moritz.diehl@imtek.uni-freiburg.de

[2]Kiteswarms GmbH, 79427 Eschbach, Germany. thilo@kiteswarms.com, reinhart@kiteswarms.com

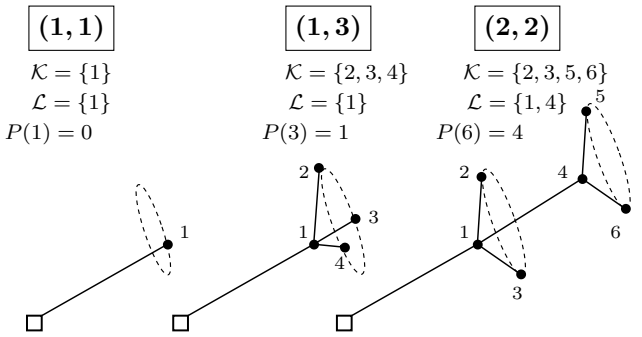

Fig. 1: Illustration of the topology of a single-kite (left), triple-kite (middle) and two-layer-dual-kite (right) AWE system.

A. Topology

The general system configuration is represented by a tree-structured topology. The trees are parametrized by nodes $n \in \mathcal{N}$, where each node represents a tether end-point. The tethers are assumed to be rigid and straight, which is a good assumption if tether tension is high. Some of the nodes $k \in \mathcal{K}$ have kites attached to them, while some nodes $l \in \mathcal{L}$ are *layer* nodes, with $\mathcal{L} := \mathcal{N} \backslash \mathcal{K}$ if $|\mathcal{N}| > 1$ and $\mathcal{L} := \mathcal{N}$ otherwise. The parent map $P(n)$ defines the interlinkage between nodes, and the children map $C(n)$ returns the set of nodes with parent n.

In this paper, we only consider the topologies that are defined by the following restrictions. The kite nodes can only be at the leaves of the tree, i.e. $P(n) \notin \mathcal{K}$ for all $n \in \mathcal{N}$. Every layer node can be the parent of only one other layer node, i.e. $|C(l) \backslash \mathcal{K}| \leq 1$ for all $l \in \mathcal{L}$. And if $|\mathcal{N}| > 1$, every layer node has the equal amount of kite children, which must be greater than one, i.e. $|C(l) \backslash \mathcal{L}| = |C(j) \backslash \mathcal{L}| > 1$ for all $l, j \in \mathcal{L}$.

Given these restrictions, every possible specific configuration is uniquely determined by the pair $(|\mathcal{L}|, \frac{|\mathcal{K}|}{|\mathcal{L}|})$, i.e. by the number of *layers* and by the number of *kites per layer*. Fig. 1 illustrates the proposed notation for some typical examples.

B. System dynamics

The dynamic equations of the system are established using an optimization-friendly modeling procedure based on non-minimal coordinates [4]. For given sets $\mathcal{N}$, $\mathcal{K}$ and parent map P, the complete system dynamics are summarized by the parametric index-1 DAE

$$\mathbf{F}(\dot{\mathbf{x}}, \mathbf{x}, \mathbf{u}, \mathbf{z}, \boldsymbol{\theta}, \mathbf{p}) = 0 \ , \tag{1}$$

with associated consistency conditions $\mathbf{C}(\mathbf{x}) = 0$.

The differential states $\mathbf{x} := (\mathbf{q}, \dot{\mathbf{q}}, \mathbf{R}, \boldsymbol{\omega}, \boldsymbol{\delta}, l_\mathrm{t}, \dot{l}_\mathrm{t}, \ddot{l}_\mathrm{t})$ firstly contain $\mathbf{q}$ and $\dot{\mathbf{q}}$ that are concatenations of the node positions $\mathbf{q}_n \in \mathbb{R}^3$ and velocities $\dot{\mathbf{q}}_n \in \mathbb{R}^3$ respectively. These are followed by the states specific to kite nodes, namely $\mathbf{R}, \boldsymbol{\omega}, \boldsymbol{\delta}$, which are concatenations of all $\boldsymbol{R}_k, \boldsymbol{\omega}_k, \boldsymbol{\delta}_k$. Aircraft orientation is represented by direct cosine matrices $\mathbf{R}_k := [\hat{\mathbf{e}}_{1,k}, \hat{\mathbf{e}}_{2,k}, \hat{\mathbf{e}}_{3,k}] \in \mathbb{R}^3$ that contain the chord-wise, span-wise and upwards unit vectors of the aircraft body frames, expressed in the inertial frame $\{\mathbf{e}_\mathrm{x}, \mathbf{e}_\mathrm{y}, \mathbf{e}_\mathrm{z}\}$. All rotation matrices should be orthonormal, i.e. they are constrained to evolve on the 3D manifold defined by

$$\mathbf{c}_{\mathrm{R},k} := P_\mathrm{ut}(\mathbf{R}_k^\top \mathbf{R}_k - I) = 0, \tag{2}$$

where the operator P_ut is used to select the upper triangular elements of a matrix. The aircraft angular velocities $\boldsymbol{\omega}_k \in \mathbb{R}^3$ are given in the body frame. The surface deflections $\boldsymbol{\delta}_k = [\delta_{\mathrm{a},k}, \delta_{\mathrm{e},k}, \delta_{\mathrm{r},k}] \in \mathbb{R}^3$ of aileron, elevator and rudder respectively, give control over the aircraft aerodynamics. Finally, tether length $l_\mathrm{t} \in \mathbb{R}$, speed $\dot{l}_\mathrm{t} \in \mathbb{R}$ and acceleration $\ddot{l}_\mathrm{t} \in \mathbb{R}$ describe the main tether reel-in and -out evolution.

The controls $\mathbf{u} := (\dot{\boldsymbol{\delta}}, \dddot{l}_\mathrm{t})$ are given by the concatenation of all aircraft surface deflection rates $\dot{\boldsymbol{\delta}}_k \in \mathbb{R}^3$ and by the tether jerk $\dddot{l}_\mathrm{t} \in \mathbb{R}$.

The algebraic variables $\mathbf{z} := (\boldsymbol{\lambda}, \boldsymbol{a})$ describe firstly the concatenation of all lagrange multipliers $\lambda_n \in \mathbb{R}$ related to the tether constraints that restrict the position of each node $n \in \mathcal{N}$ to evolve on a 2D manifold defined by

$$c_n := \frac{1}{2}\left((\mathbf{q}_n - \mathbf{q}_{P(n)})^\top (\mathbf{q}_n - \mathbf{q}_{P(n)}) - l_n^2\right) = 0 \ , \tag{3}$$

where $\mathbf{q}_0$ lies in the origin, and where l_n is the tether length associated with node n. The first tether length is that of the main tether, i.e. $l_1 := l_\mathrm{t}$. If $|\mathcal{N}| > 1$, then the lengths of the secondary tethers $l_k := l_\mathrm{S}$ for $k \in \mathcal{K}$ and the lengths of the layer-linking tethers $l_l := l_\mathrm{i}$ for $l \in \mathcal{L} \backslash \{1\}$. The variables a_l, one for each layer $l \in \mathcal{L}$, are concatenated in the vector $\boldsymbol{a}$. They represent the instantaneous induction factors, further described in section II-D.

The variables $\boldsymbol{\theta} := (\boldsymbol{l}, \boldsymbol{d})$ contain concatenations of the key system parameters that can be optimized over. The vector $\boldsymbol{l} := l_\mathrm{S}$ if $|\mathcal{N}| > 1$ and empty otherwise. The vector $\boldsymbol{d}$ constains the main tether diameter d_T, the secondary tether diameters d_S if $|\mathcal{N}| > 1$ and the intermediate tether diameter d_I if $|\mathcal{L}| > 1$.

The constant parameters $\mathbf{p} := (b, u_\mathrm{ref}, z_\mathrm{ref}, z_0)$, allow the dynamics to be evaluated for different aircraft wing spans b and different wind profile parameters $u_\mathrm{ref}, z_\mathrm{ref}, z_0$, as further described below.

C. Lagrangian dynamics

In accordance with the Lagrangian approach proposed in [4], the system Lagrangian can be defined as

$$L := \sum_n^{\mathcal{N}} (T_n - V_n - \lambda_n c_n) \ , \tag{4}$$

with for each node $n \in \mathcal{N}$ the kinetic energy T_n and potential energy V_n given by

$$T_n := \frac{1}{2} m_n \dot{\mathbf{q}}_n^\top \dot{\mathbf{q}}_n + \frac{1}{2} \boldsymbol{\omega}_n^\top J_\mathrm{K} \boldsymbol{\omega}_n \delta_{(n \in \mathcal{K})} \tag{5}$$

$$V_n := m_n g \mathbf{q}^\top \mathbf{e}_\mathrm{z} \ . \tag{6}$$

Here, the mass of each node is defined as

$$m_n := m_\mathrm{K} \delta_{(n \in \mathcal{K})} + \frac{1}{2} \rho_\mathrm{t} (d_n^2 l_n + \sum_c^{C(n)} d_c^2 l_c) \frac{\pi}{4} \ . \tag{7}$$

Note that each node carries half of the weight of each tether that is linked to it. Here, m_{K} and J_{K} are the aircraft mass and moment of inertia respectively. The variable $\delta_{(n\in\mathcal{K})}$ equals 1 for kite nodes and 0 for tether nodes. Finally, ρ_{t} is the tether material density.

The translational dynamics are readily given by

$$\frac{\mathrm{d}}{\mathrm{d}t}\frac{\partial L}{\partial \dot{\mathbf{q}}} - \frac{\partial L}{\partial \mathbf{q}} = \mathbf{F} + \mathbf{F}_{\mathrm{mom}} \tag{8}$$

with $\mathbf{F}$ the concatenation of the external forces $\mathbf{F}_n$ exerted on each of the nodes. The term

$$\mathbf{F}_{\mathrm{mom}} := \sum_{n}^{\mathcal{N}} \frac{\mathrm{d}m_n}{\mathrm{d}t}\dot{\mathbf{q}}_n^{\top}\frac{\partial \dot{\mathbf{q}}_n}{\partial \dot{\mathbf{q}}} \tag{9}$$

is a momentum correction that takes into account the fact that over time mass is added to and extracted from the airborne part of the tether due to reel-in and -out.

Following [4] the rotational dynamics can be projected on a 3D manifold so as to read:

$$J_{\mathrm{K}}\frac{\mathrm{d}\boldsymbol{\omega}_k}{\mathrm{d}t} + \boldsymbol{\omega}_k \times J_{\mathrm{K}}\boldsymbol{\omega}_k = \mathbf{M}_k \ , \tag{10}$$

with $\mathbf{M}_k$ the aerodynamic moment exerted on the aircraft.

An index reduction combined with a Baumgarte stabilization scheme [3] is performed on the holonomic tether constraints so that they are imposed as

$$\ddot{c}_n + 2\kappa\dot{c}_n + \kappa^2 c_n = 0 \ , \tag{11}$$

were κ is a tuning parameter.

The same stabilization technique is applied to the rotational kinematics:

$$\frac{\mathrm{d}\mathbf{R}_k}{\mathrm{d}t} = \mathbf{R}_k\left(\frac{\kappa_{\mathrm{R}}}{2}(I - \mathbf{R}_k^{\top}\mathbf{R}_k) + \mathrm{skew}(\boldsymbol{\omega}_k)\right) \tag{12}$$

with κ_{R} another tuning parameter.

Performing Baumgarte stabilization on the system invariants in the context of periodic optimal control will not only ensure that the consistency conditions $\mathbf{C}(\mathbf{x}) := (\mathbf{c}, \dot{\mathbf{c}}_n, \mathbf{c}_{\mathrm{R}}) = 0$ are satisfied over the entire time interval, but also preserves linear independence of the optimization constraints [5]. The variables $\mathbf{c}, \dot{\mathbf{c}}_n$ and $\mathbf{c}_{\mathrm{R}}$ denote the concatenations of all c_n and $\dot{c}_n$ for all $n \in \mathcal{N}$, and all $\mathbf{c}_{\mathrm{R},k}$ for all $k \in \mathcal{K}$ respectively.

The trivial kinematics

$$\frac{\mathrm{d}}{\mathrm{d}t}(\mathbf{q}, \boldsymbol{\delta}, l_{\mathrm{t}}, \dot{l}_{\mathrm{t}}) = (\dot{\mathbf{q}}, \dot{\boldsymbol{\delta}}, \dot{l}_{\mathrm{t}}, \ddot{l}_{\mathrm{t}}) \tag{13}$$

together with (8) - (12) then give the system dynamics summarized by (1), save for expressions for the aerodynamic forces $\mathbf{F}_n$ and moments $\mathbf{M}_k$, as well as the algebraic equations that determine the layer induction factors $\mathbf{a}$.

D. Aerodynamic model

Due to wind shear in the atmospheric boundary layer, the available wind power can grow significantly with increasing altitude. A commonly used model assumes both steady flow conditions and a logarithmic profile for the freestream wind velocity [2]:

$$\mathbf{u}_\infty(z) := u_{\mathrm{ref}}\frac{\log\frac{z}{z_0}}{\log\frac{z_{\mathrm{ref}}}{z_0}}\mathbf{e}_{\mathrm{x}} \ . \tag{14}$$

In this approximation, u_{ref} is the reference wind speed that is measured at an altitude z_{ref}, whereas z_0 is the surface roughness length. The atmospheric density drop $\rho(z)$ is taken into account using the international standard atmosphere model and the parameters found in [2].

Tether drag forces and kite aerodynamics are modeled in identical fashion as in [8], and the reader is referred to this paper for both the explicit expressions and the values of the aerodynamic coefficients. The tether drag of each segment is computed at the midpoint and distributed equally between the nodes it connects. This is a computationally inexpensive approximation that however underestimates the tether drag at the kite nodes. The aircraft aerodynamics are described by stability derivatives, based on the apparent wind velocity $\mathbf{u}_{\mathrm{a},k}$. The aerodynamic coefficients correspond to those identified for the existing Ampyx AP2 system, which is chosen here as a reference aircraft [10]. It has a mass m_{ref} and an inertia tensor J_{ref}. The equations given in [8] are summarized here as:

$$\mathbf{F}_n := \mathbf{f}_{\mathrm{F},n}(\mathbf{x}, \mathbf{z}, \boldsymbol{\theta}, \mathbf{p}) \ , \tag{15}$$

$$\mathbf{M}_k := \mathbf{f}_{\mathrm{M},k}(\mathbf{x}, \mathbf{z}, \boldsymbol{\theta}, \mathbf{p}) \ , \tag{16}$$

for $n \in \mathcal{N}$ and $k \in \mathcal{K}$.

The actuator-disk method (AD) used to approximate induction effects is based on the one presented in [8]. It assumes steady potential flow that is in equilibrium. Based on conservation of momentum considerations, $|\mathcal{L}|$ algebraic equations are derived:

$$4a_l\dot{l}_{\mathrm{t}} - C_{\mathrm{T}}\|\mathbf{u}_\infty(\mathbf{e}_{\mathrm{z}}^{\top}\mathbf{q}_{\mathrm{c},l})\|_2 = 0 \ , \tag{17}$$

each of them determining an instantaneous induction factor a_l, for $l \in \mathcal{L}$. Here $\mathbf{q}_{\mathrm{c},l} := \sum_k^{C(l)}\mathbf{q}_k/|C(l)|$ is the arithmetic center of the aircraft. The thrust coefficient is defined as $C_{\mathrm{T}} := \sum_k^{C(l)}\mathbf{n}_l^{\top}\mathbf{F}_k/(\mathbf{q}'_{0,l}A_l)$. The actuator normal vector is given by $\mathbf{n}_l := (\mathbf{q}_l - \mathbf{q}_{P(l)})/\|\mathbf{q}_l - \mathbf{q}_{P(l)}\|_2$. The aerodynamic pressure at the actuator center is defined as $\mathbf{q}'_{0,l} := 1/2\rho(\mathbf{e}_{\mathrm{z}}^{\top}\mathbf{q}_{\mathrm{c},l})\|\mathbf{u}_\infty(\mathbf{e}_{\mathrm{z}}^{\top}\mathbf{q}_{\mathrm{c},l}) - \mathbf{u}_{\mathrm{act},l}\|_2$, with the actuator velocity $\mathbf{u}_{\mathrm{act},l} := \sum_k^{C(l)}\dot{\mathbf{q}}_k/|C(l)|$. The actuator area A_l is modeled as an annulus, so that $A_l := 2\pi b\|\mathbf{d}'_l - (\mathbf{n_l}^{\top}\mathbf{d}'_l)\mathbf{n}_l\|_2$, with the average distance w.r.t. the actuator center $\mathbf{d}'_l := \sum_k^{C(l)}(\mathbf{q}_k - \mathbf{q}_{\mathrm{c},l})/|C(l)|$. The apparent wind velocity of kite k is then given by

$$\mathbf{u}_{\mathrm{a},k} := \mathbf{u}_\infty(\mathbf{e}_{\mathrm{z}}^{\top}\mathbf{q}_{\mathrm{c},P(k)}) - \dot{\mathbf{q}}_k + \mathbf{u}_{\mathrm{ind},k} \ , \tag{18}$$

with $\mathbf{u}_{\mathrm{ind},k} := -a_{P(k)}\|\mathbf{u}_\infty(\mathbf{e}_{\mathrm{z}}^{\top}\mathbf{q}_{\mathrm{c},P(k)}) - \mathbf{u}_{\mathrm{act},P(k)}\|_2\mathbf{n}_{P(k)}$. The wake of each layer is assumed to behave independently. This is done to limit computational complexity, though it is only a good assumption when the distance between the layers is large in comparison to the flight radius. In this study, the length l_{i} is assumed to take a constant value of $100\ \mathrm{m}$, which is arguably small. However, increasing this value does not change the system power output significantly.

E. System upscaling

In order to evaluate the system dynamics for different wing spans b, the following mass scaling law is assumed to hold when upscaling the reference aircraft:

$$m_{\mathrm{K}} := m_{\mathrm{ref}} \left(\frac{b}{b_{\mathrm{ref}}}\right)^{\kappa} \quad \text{and} \quad J_{\mathrm{K}} := J_{\mathrm{ref}} \left(\frac{b}{b_{\mathrm{ref}}}\right)^{\kappa+2} . \tag{19}$$

For simplicity, we assume that the wing aspect ratio AR remains constant. The exponent $\kappa = 2.4$ slightly underestimates the upscaling law implicit in the data presented in [7]. The values of the aircraft stability derivatives are kept constant for different aircraft sizes, under the assumption of identical geometry and low Reynold's number variation. This assumption is violated in the results below, hence the resulting data are therefore not suited for making actual design decisions for real systems.

F. Constraints

The system path constraints

$$\mathbf{h}(\dot{\mathbf{x}}, \mathbf{x}, \mathbf{u}, \mathbf{z}, \boldsymbol{\theta}, \mathbf{p}) \leq 0 \ , \tag{20}$$

firstly entail that the tether stress of all tethers should be limited below some critical value:

$$\tau_n f_{\mathrm{s}} - s_n \sigma_{\max} \leq 0 \ , \tag{21}$$

where f_{s} is a safety factor, $\tau_n := \lambda_n l_n$ is the tension force of tether n and $s_n := \pi \frac{d_n^2}{4}$. The parameter $\sigma_{\max}$ is the maximum allowed tether stress.

Furthermore, kite accelerations are limited to a hardware-friendly range defined by

$$\|\ddot{\mathbf{q}}_k\|_2 \leq a_{\max} \ . \tag{22}$$

All kites have to to keep a safety distance $f_{\mathrm{b}} b$ from each other, which is formulated as

$$\|\mathbf{q}_i - \mathbf{q}_j\|_2 - f_{\mathrm{b}} b \leq 0 \ , \tag{23}$$

for all pairs $(i, j) \in \mathcal{K} \times \mathcal{K}$, with $f_{\mathrm{b}} = 5$.

In order to ensure model validity and to prevent stall, the kites' angle of attack α_k and side slip β_k are bounded to stay within the intervals $[\alpha_{\min}, \alpha_{\max}]$ and $[\beta_{\min}, \beta_{\max}]$ respectively, as explicitly stated in [8]. Finally the kites' orientation is constrained to provent collision with the tether. Let $\hat{\mathbf{q}}_k = \mathbf{q}_k - \mathbf{q}_{P(k)}$. The orientation constraint then reads as

$$\sin(\theta_{\min}) \leq -\frac{\hat{\mathbf{q}}_k^{\top} \hat{\mathbf{e}}_{1,k}}{\|\hat{\mathbf{q}}_k\|_2} \leq \sin(\theta_{\max}) \tag{24}$$

$$\tan(\phi_{\min}) \leq \frac{\hat{\mathbf{q}}_k^{\top} \hat{\mathbf{e}}_{2,k}}{\hat{\mathbf{q}}_k^{\top} \hat{\mathbf{e}}_{3,k}} \leq \tan(\phi_{\max}), \tag{25}$$

with the corresponding bounds on the pitch and roll angles θ and ϕ. The reader is referred to [8] for a full overview of system parameters and variable bounds used. The maximum tether length is set to 5 km. In this study, we abstract from the economical consequences (e.g. on the packing density for a farm configuration) of allowing such a long tether. Tether elasticity has been neglected in this study.

III. PROBLEM FORMULATION AND SOLUTION

Periodic optimal control is applied to compute feasible power-optimal periodic flight trajectories of free time period T. In the periodic optimal control problem (OCP), the initial state and terminal state can be chosen freely but must be equal:

$$\mathbf{x}(0) - \mathbf{x}(T) = 0 \ . \tag{26}$$

In order to remove phase invariance from the problem, as well as to avoid multiple periodic orbits within one solution, the following phase-fix strategy is adopted. Consider a time period T_1 for the reel-in phase, and one T_2 for the reel-out phase. The overall cycle time is thus defined as $T := T_1 + T_2$. Then, reel-out and reel-in phase are uniquely determined by introducing the constraints

$$\dot{l}_{\mathrm{t}}(t) \geq 0, \ \forall t \in [0, T_1] \ \text{ and } \dot{l}_{\mathrm{t}}(t) \leq 0, \ \forall t \in [T_1, T] \ . \tag{27}$$

Using the system dynamics and constraints described in section II, the following OCP can be solved to locally maximize the rated power output $\bar{P}$, for a given configuration with sets $\mathcal{K}, \mathcal{L}$ and for given parameters $\mathbf{p}$:

$$\begin{aligned} \bar{P}(\mathbf{w}^*, \mathbf{p}) := \ & \max_{\mathbf{w}} \ \frac{1}{T} \int_0^T \hat{P}(t) \mathrm{d}t \\ & \text{s.t.} \quad (1), (20), (26) - (27) \end{aligned} \tag{28}$$

Here $\hat{P} := \lambda_1 l_{\mathrm{t}} \dot{l}_{\mathrm{t}}$ is the instantaneous mechanical power transferred to the ground station by the main tether. The decision variables are defined as $\mathbf{w} := (\mathbf{x}(\cdot), \mathbf{u}(\cdot), \mathbf{z}(\cdot), \boldsymbol{\theta}, T_1, T_2)$.

The OCP (28) is discretized in $10 \cdot N_{\mathrm{loop}}$ intervals using direct collocation with Radau polynomials of order 4. The initial guess for the resulting NLP is found by a homotopy procedure, that involves solving a series of problems of increasing non-linearity, starting from the tracking of N_{loop} circular loops. The NLP is formulated using the symbolic modeling language and framework for algorithmic differentation CasADi [1] in Python, and solved with the interior-point solver IPOPT [15] and the linear solver MA57 [6]. The resulting NLP size ranges from 3565 variables, 3384 equality and 800 inequality constraints for configuration $(1, 1)$ to 19527 variables, 18447 equality and 6480 inequality constraints for configuration $(3, 2)$. The problems are solved on an Intel Core i7 2.5 Ghz, 16GB RAM. Computation times range from 30 seconds for configuration $(1, 1)$ up to more than 3 hours for configuration $(3, 2)$.

IV. RESULTS

In order to assess the potential of the stacked multi-kite configuration for utility-scale AWE, we carry out a case study at two types of wind site. Each wind site has a specific rated *mechanical* power demand P_{nom}, as summarized in Table I. For each wind site, and for each considered configuration with sets $\mathcal{K}, \mathcal{L}$, the optimal control problem (28) is solved for different wing spans b until the average power output $\bar{P}(\mathbf{w}^*, \mathbf{p}_{\mathrm{nom}}) \approx P_{\mathrm{nom}}$, with the corresponding system parameters $\mathbf{p}_{\mathrm{nom}} = (b_{\mathrm{nom}}, u_{\mathrm{ref}}, z_{\mathrm{ref}}, z_0)$.

TABLE I: Case study parameters

Quantity	P_{nom}	u_{ref}	z_{ref}	z_0
Units	MW	m/s	m	m
Offshore	4	10	94	0.0002
Onshore	2	8.5	94	0.1

A. Trajectory analysis

The solution of (28) cannot be guaranteed to be a global one, but for all stacked multi-kite configurations the trajectories seem reasonable. They are qualitatively very similar to the dual-kites pumping cycles obtained in [8]. Fig. 2 shows as an example the trajectory of the $(3,2)$ configuration. It consists of $N_{\text{loop}} = 2$ loops of crosswind flight during reel-out and a straight flight back outwards during reel-in so as to minimize the force in the direction of the main tether.

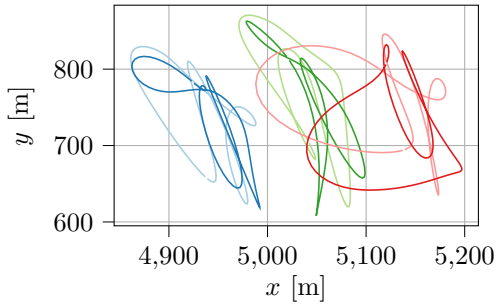

(a) Side view.

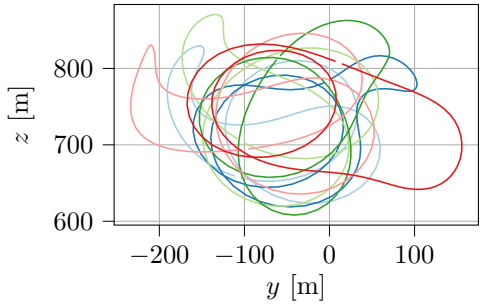

(b) Upstream view.

Fig. 2: Optimal kite node trajectories of the $(3,2)$ configuration in the 4 MW offshore case.

In the offshore case, there is a big increase in flying height (from roughly 200 m to 500 m) in the transition from single to dual kites, as Fig. 3 shows. This is explained by the reduced main tether drag and confirms the results obtained in [16]. Due to the low offshore wind speed gradient, it becomes at some point inefficient for the dual kites to carry more tether mass in order to fly higher. As stacked systems tap into a larger overall harvesting area they can carry more mass and will fly higher (up to 750 m for the $(3,2)$ configuration). In the onshore case, not shown here, all multi-kite systems fly at the maximum tether length due to the higher velocity gradient.

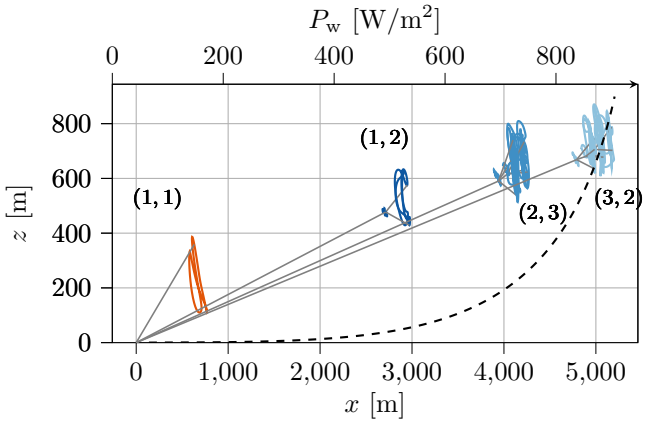

Fig. 3: Side view of node position trajectories for different configurations of the 4 MW offshore case. The dashed line displays the wind power density $P_{\text{w}}(z) := \frac{1}{2}\rho(z)\|\mathbf{u}_\infty(z)\|_2^3$.

Apart from an increased flying height, stacked configurations result in a lower peak power overshoot and a more constant power output. Stacked configurations naturally distribute the amount of mass flying upwards more evenly over one revolution, as they are composed of lighter and spatially more distributed aircraft. Different layers can phase their rotation w.r.t. each other in order to obtain an optimal distribution. Fig. 4 shows how the peak power output is systematically reduced as kites and layers are added to the configuration. The configuration $(3,2)$ achieves a 59% reduction in peak power compared to single kite systems, and a 27% reduction compared to dual kites. This is the only configuration that displays a period of constant power output.

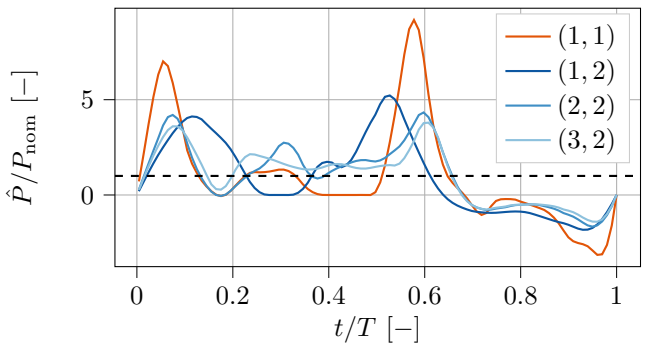

Fig. 4: Normalized instantaneous power output profiles for different configurations in the 4MW offshore case.

B. System sizing

The different required wing spans b_{nom} for considered configurations are given in Fig. 5a, whereas Fig. 5b gives the power output per total aerodynamic surface area $\bar{P}_{\text{S}} := \bar{P}/\sum_k^{\mathcal{K}} S_k$, which is taken here as a measure of system efficiency.

The first thing to observe is that the wing span of configuration $(1, 2)$ is about half that of configuration $(1, 1)$, since the first is able to fly at much larger altitude. The power-per-surface-area is significantly increased (50% for the offshore case), which is in line with the findings in [16]. Notice that the effect is more pronounced in the onshore case, as the wind speed gradient with altitude is larger.

The second observation is that in order to maximize efficiency, a fixed number of aircraft should always be distributed over as many layers as possible. This strategy maximizes the amount of available harvesting area. Compare for example systems $(1, 4)$ and $(2, 2)$, for both of which $|\mathcal{K}| = 4$. The latter has roughly twice the available harvesting area as the first, resulting in a significantly higher efficiency: 20% more power per surface area offshore.

Finally, the results in Fig. 5a show how extending the design space to stacked configurations effectively decouples aircraft sizing from demanded power output. For example, assume that it would be particularly cost-effective to mass-produce an aircraft with 21 m wing span. Then, one could employ the same aircraft type, with minor adaptations, for a 2 MW onshore site in a $(1, 3)$ configuration as well as for a 4 MW offshore wind site in a $(2, 3)$ configuration. Higher power output demands could be met by opting for configurations with even more layers. Reversely, one could meet a specific power demand with a whole range of aircraft sizes, that could then be dimensioned mainly on economic criteria. The negative slopes in Fig. 5a suggest that this range could be extended to even smaller aircraft than those considered in this study.

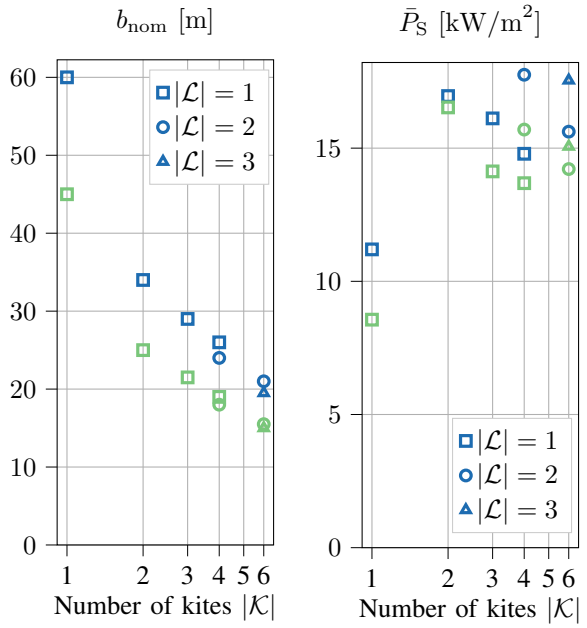

(a) (b)

Fig. 5: Wing span (a) and power per aerodynamic surface area (b) for different configurations in the 4MW offshore case (blue) and 2MW onshore case (green).

V. CONCLUSIONS

In this paper, an upscaling strategy for airborne wind energy based on stacked multi-kite systems has been proposed. It has been shown in two industry-relevant case studies that this modular strategy can effectively render aircraft wing sizing considerations largely independent from the rated power demand of a specific wind site.

Future research will focus on developing fast models that describe the wake interaction between different stacking layers. Launch-and-landing strategies for stacked multi-kite systems are the subject of ongoing research.

ACKNOWLEDGMENTS

This research was supported by an industrial project with the company Kiteswarms Ltd, by DFG via Research Unit FOR 2401, by the German Federal Ministry for Economic Affairs and Energy (BMWi) via eco4wind (0324125B) and DyConPV (0324166B).

REFERENCES

[1] J. A. E. Andersson, J. Gillis, G. Horn, J. B. Rawlings, and M. Diehl. CasADi: a software framework for nonlinear optimization and optimal control. *Mathematical Programming Computation*, 2018.

[2] C. Archer. An introduction to meteorology for airborne wind energy. In *Airborne Wind Energy*. Springer Berlin / Heidelberg, 2013.

[3] J. Baumgarte. Stabilization of Constraints and Integrals of Motion in Dynamical Systems. *Computer Methods in Applied Mechanics and Engineering*, 1(1):1–16, 1972.

[4] S. Gros and M. Diehl. Modeling of airborne wind energy systems in natural coordinates. In *Airborne Wind Energy*. Springer-Verlag Berlin Heidelberg, 2013.

[5] S. Gros and M. Zanon. Numerical optimal control with periodicity constraints in the presence of invariants. *IEEE Transactions on Automatic Control (under revision)*, 2018.

[6] HSL. A collection of Fortran codes for large scale scientific computation. `http://www.hsl.rl.ac.uk`, 2011.

[7] M. Kruijff and R. Ruiterkamp. A roadmap towards airborne wind energy in the utility sector. In *Airborne Wind Energy: Advances in Technology Development and Research*. Springer, Singapore, 2018.

[8] R. Leuthold, J. De Schutter, E. Malz, G. Licitra, S. Gros, and M. Diehl. Operational regions of a multi-kite awe system. In *European Control Conference (ECC)*, 2018.

[9] R. Leuthold, S. Gros, and M. Diehl. Induction in optimal control of multiple-kite airborne wind energy systems. In *Proceedings of 20th IFAC World Congress, Toulouse, France*, 2017.

[10] G. Licitra, P. Williams, J. Gillis, S. Ghandchi, S. Sieberling, R. Ruiterkamp, and M. Diehl. Aerodynamic parameter identification for an airborne wind energy pumping system. In *Proceedings of the IFAC World Congress*, 2017.

[11] M. Loyd. Crosswind Kite Power. *Journal of Energy*, 4(3):106–111, July 1980.

[12] Makani Power Inc. Response to the federal aviation authority. Technical report, 2017.

[13] P. Payne and C. McCutchen. Self-Erecting Windmill. United States Patent 3987987, Oct. 26 1976.

[14] R. Read. Kite networks for harvesting wind energy. In *Airborne Wind Energy: Advances in Technology Development and Research*. Springer Singapore, 2018.

[15] A. Wächter and L. T. Biegler. On the implementation of an interior-point filter line-search algorithm for large-scale nonlinear programming. *Mathematical Programming*, 106(1):25–57, 2006.

[16] M. Zanon, S. Gros, J. Andersson, and M. Diehl. Airborne wind energy based on dual airfoils. *IEEE Transactions on Control Systems Technology*, 21:1215–1222, July 2013.

[17] M. Zanon, S. Gros, J. Meyers, and M. Diehl. Airborne wind energy: Airfoil-airmass interaction. In *Proceedings of the IFAC World Congress*, pages 5814–5819, 2014.